Exploration Geophysics

ISSN: 0812-3985 (Print) 1834-7533 (Online) Journal homepage: https://www.tandfonline.com/loi/texg20

Three-dimensional magnetotelluric modelling in anisotropic media using the A-phi method

Tiaojie Xiao, Xiangyu Huang & Yun Wang

To cite this article: Tiaojie Xiao, Xiangyu Huang & Yun Wang (2019): Three-dimensional magnetotelluric modelling in anisotropic media using the A-phi method, Exploration Geophysics, DOI: 10.1080/08123985.2018.1564274

To link to this article: https://doi.org/10.1080/08123985.2018.1564274

Published online: 07 Feb 2019.

EXPLORATION GEOPHYSICS
https://doi.org/10.1080/08123985.2018.1564274

Taylor & Francis
Taylor & Francis Group

Three-dimensional magnetotelluric modelling in anisotropic media using the A-phi method

Tiaojie Xiao[a,b], Xiangyu Huang[c] and Yun Wang[a]

[a]Institute of Geochemistry, Chinese Academy of Sciences, Guiyang, China; [b]University of Chinese Academy of Sciences, Beijing, China; [c]School of Geosciences and Info-Physics, Central South University, Changsha, China

ABSTRACT

It is important to study the responses of the magnetotelluric (MT) method in anisotropic media. However, MT anisotropy research has focused mainly on one-dimensional (1D) and two-dimensional (2D) solutions. Therefore, we developed a three-dimensional (3D) finite element (FE) algorithm for MT modelling in anisotropic media. This approach is based on the weak formulation of the governing Maxwell equations using Coulomb-gauged potentials. The node-based FE method is adopted here, and the values of the coefficient matrixes are obtained with hexahedral meshes. To validate the correctness and accuracy of this method, its results are compared with previous solutions for a 2D anisotropic model and a 3D arbitrary anisotropic model, respectively. Different solvers with different preconditioners are tested, and the results show that the quasi-minimum residual method with the incomplete LU preconditioner is more stable and faster compared with the other schemes. We then studied a 3D anisotropic model in three different conditions, and analysed the results in detail. Finally, three main conclusions are obtained: the xy- and yy-mode apparent resistivities remain almost unchanged if a principal conductivity is in the *x*-direction; the yx- and xx-mode apparent resistivities remain almost the same if a principal conductivity is in the *y*-direction; a principal conductivity in the *z*-direction has almost no influence on apparent resistivities.

ARTICLE HISTORY
Received 10 July 2017
Accepted 19 December 2018

KEYWORDS
Magnetotelluric; anisotropy; 3D modelling; Coulomb-gauged potentials; finite element

Introduction

The magnetotelluric (MT) method, a passive geophysical exploration technique, has been used in many areas such as mineral resources surveys, oil and gas exploration, and investigation of deep Earth electrical structures (Farquharson and Craven 2009; Bai et al. 2010; Sarvandani et al. 2017). Researchers (Christensen 1984; Klein and Santamarina 2003; Evans et al. 2005) have shown that the Earth is anisotropic, and electrical anisotropy has been recognised as a significant factor for the interpretation of MT data. Although it is not reasonable to ignore the anisotropic influence, interpretations of MT data generally assume that the medium is isotropic. Because modelling is the base of the inversion, it is meaningful and important to study MT modelling in anisotropic media.

In one-dimensional (1D) anisotropic media, forward modelling and inversion of MT have been widely studied (O'Brien et al. 1967; Reddy and Rankin 1971; Dekker and Hastie 1980; Yin 2000; Pek and Santos 2002; Kirkby et al. 2015). A great many of studies (Heise and Pous 2001, 2003; Yin 2003; Hu et al. 2013; Huo et al. 2015) of two-dimensional (2D) anisotropic media have also been carried out: early research focused on symmetrical anisotropic media (Xu 1994); Pek and Verner (1997) developed the finite difference (FD) method for MT modelling in 2D arbitrary anisotropic media; later, Li (2002) presented a 2D finite element (FE) method for MT modelling in generalised anisotropic media; and Li and Pek (2008) further developed a 2D adaptive FE modelling algorithm in arbitrary anisotropic media. However, despite the great deal of work carried out in this general area, there are just a handful of three-dimensional (3D) anisotropic modelling studies (Martinelli and Osella 1997; Wang and Fang 2001; Häuserer and Junge 2011; Löwer and Junge 2017; Kong et al. 2018; Cao et al. 2018). In particular, Weidelt et al. (1999) presented a staggered-grid FD algorithm for MT modelling in 3D arbitrary anisotropic media, however, this algorithm is not convenient for dealing with irregular anomalies. Li (2000) presented a node-based FE method for MT modelling, however, it is not accurate enough because the nodal FE method cannot meet the required condition that the normal electric fields are discontinuous at electrical interfaces. To avoid this disadvantage of the node-based FE method, Xiao et al. (2018b) developed an edge-based FE method, but it is also not convenient for dealing with irregular anomalies or topography as rectangular meshes were adopted. Recently, Liu et al. (2018) presented an adap-

CONTACT Tiaojie Xiao xiaotiaojie16@mails.ucas.ac.cn Institute of Geochemestry, Chinese Academy of Sciences, 99 Lincheng Road, Guiyang, Guizhou 550081, China

tive FE method with tetrahedron elements in 3D general anisotropic media, which is able to simulate topography and irregular anomalies.

FE methods are widely used in the area of electromagnetic (EM) numerical modelling (Everett 2012; Cai et al. 2014; Ren et al. 2014; Li et al. 2016). For MT modelling, most of the FE methods are formulated in terms of electric fields or magnetic fields, although they can also be formulated in terms of coupled vector–scalar potentials (Biro and Preis 1989; Haber et al. 2000; Badea et al. 2001; Mitsuhata and Uchida 2004; Xiao et al. 2018). Puzyrev et al. (2013) presented a nodal FE algorithm for 3D controlled-source EM (CSEM) forward modelling problems using the secondary coupled-potential formulation of Maxwell's equations in anisotropic media, however, the case of generalised anisotropy was not taken into consideration. Cai et al. (2015) implemented a 3D FE solution for marine CSEM data and formulated the problem with the scalar and vector potentials, but also did not consider generalised anisotropy.

Here, the algorithm for 3D MT forward modelling in anisotropic media is formulated in terms of Coulomb-gauged EM potentials ($\mathbf{A}-\psi$) using a node-based FE method. The main contribution of this paper is that we develop a method to simulate MT responses in 3D electrical anisotropic media. Although there are several algorithms in terms of electric or magnetic fields, we present another option.

Problem formulation

Applying the MT method, displacement currents are negligible in comparison with their conduction counterparts. For the EM field, the diffusive Maxwell's equations with a time dependence of $e^{-i\omega t}$ are (Xu 1994):

$$\nabla \times \mathbf{E} = i\omega\mu\mathbf{H} \tag{1}$$

$$\nabla \times \mathbf{H} = \tilde{\sigma}\mathbf{E} \tag{2}$$

In these expressions, **E** and **H** are the EM field, ω is the angular frequency, μ is the magnetic permeability of free space, and $\tilde{\sigma}$ is the conductivity in anisotropic media. $\tilde{\sigma}$ in Equation (2) is a tensor as follows:

$$\tilde{\sigma} = \begin{pmatrix} \sigma_{xx} & \sigma_{xy} & \sigma_{xz} \\ \sigma_{yx} & \sigma_{yy} & \sigma_{yz} \\ \sigma_{zx} & \sigma_{zy} & \sigma_{zz} \end{pmatrix} \tag{3}$$

There are two methods (Yin 2000; Pek and Santos 2002) to define $\tilde{\sigma}$, the latter of which is adopted here. As shown in Figure 1, $\tilde{\sigma}$ is represented by six variables: three principal conductivities (σ_x, σ_y, σ_z), as well as the strike angle, dip angle and slant angle ($\alpha_S, \alpha_D, \alpha_L$). The rotation axes of three rotations are the z-axis, x'-axis and z'-axis, respectively.

The EM field can be expressed in terms of a magnetic vector potential **A** and an electrical scalar potential ψ as (Puzyrev et al. 2013),

$$\mathbf{B} = \nabla \times \mathbf{A} \tag{4}$$

$$\mathbf{E} = i\omega(\mathbf{A} + \nabla\psi) \tag{5}$$

where $\mathbf{B} = \mu_0\mathbf{H}$.

To guarantee the uniqueness of the vector potential **A**, the Coulomb gauge condition$\nabla \cdot \mathbf{A} = 0$ should be adopted. Substituting Equations (4) and (5) into Equations (1) and (2), then Equations (6) and (7) are obtained as follows (see Puzyrev et al. (2013) for details):

$$\nabla^2\mathbf{A} + i\omega\mu_0\tilde{\sigma}(\mathbf{A} + \nabla\psi) = 0 \tag{6}$$

$$\nabla \cdot [i\omega\mu_0\tilde{\sigma}(\mathbf{A} + \nabla\psi)] = 0 \tag{7}$$

Solving Equations (6) and (7) simultaneously with proper boundary conditions, then **A** and ψ can be obtained.

Finite element analysis

The study domain utilised here, as shown in Figure 2, is divided into two zones (the air zone and the subterranean zone).

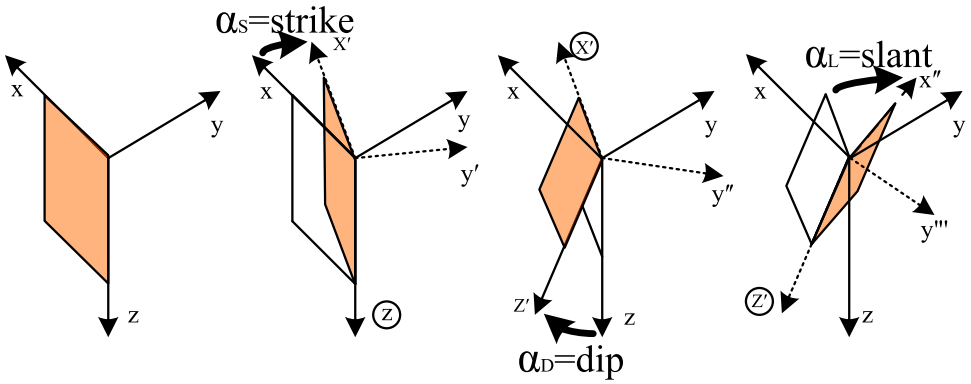

Figure 1. Illustration of basic anisotropic parameters: transformation of conductive dike into general position by successively applying three elementary Euler's rotations α_S, α_D and α_L (Pek and Santos 2002).

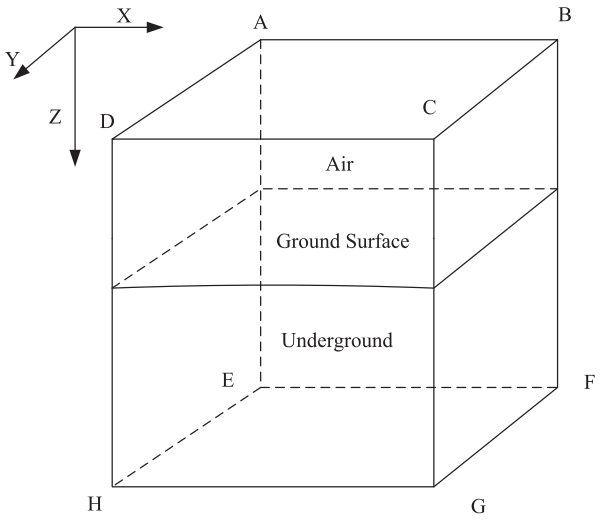

Figure 2. The solution domain.

In Cartesian coordinates, the magnetic vector potential can be written as,

$$\mathbf{A} = A_x\mathbf{e}_x + A_y\mathbf{e}_y + A_z\mathbf{e}_z \tag{8}$$

Therefore, Equations (6) and (7) can be written as,

$$\nabla^2 A_x + i\omega\mu_0\tilde{\sigma}(A_x + \frac{\partial\psi}{\partial x}) = 0 \tag{9}$$

$$\nabla^2 A_y + i\omega\mu_0\tilde{\sigma}(A_y + \frac{\partial\psi}{\partial y}) = 0 \tag{10}$$

$$\nabla^2 A_z + i\omega\mu_0\tilde{\sigma}(A_z + \frac{\partial\psi}{\partial z}) = 0 \tag{11}$$

$$i\omega\mu_0\tilde{\sigma}(\frac{\partial A_x}{\partial x} + \frac{\partial A_y}{\partial y} + \frac{\partial A_z}{\partial z}) + i\omega\mu_0\nabla\cdot[\tilde{\sigma}\nabla\psi] = 0 \tag{12}$$

A node-based FE method (Jin 2002) is used here to discretise Equation (6) and Equation (7), and considering Green's first identity (Equation 13) and the vector calculus identity (Equation 14),

$$\int_v (\nabla\phi\cdot\nabla\varphi + \phi\nabla^2\varphi)\mathrm{d}v = \oint_s (\phi\nabla\varphi)\cdot\mathbf{ds} \tag{13}$$

$$\nabla\cdot(\varphi\mathbf{A}) = \varphi(\nabla\cdot\mathbf{A}) + \mathbf{A}\cdot(\nabla\varphi) \tag{14}$$

Volume-integrated equations can be obtained as follows:

$$-(\nabla N, \nabla A_x)_\Omega + i\omega\mu_0\tilde{\sigma}\left(N, A_x + \frac{\partial\psi}{\partial x}\right)_\Omega = 0 \tag{15}$$

$$-(\nabla N, \nabla A_y)_\Omega + i\omega\mu_0\tilde{\sigma}\left(N, A_y + \frac{\partial\psi}{\partial y}\right)_\Omega = 0 \tag{16}$$

$$-(\nabla N, \nabla A_z)_\Omega + i\omega\mu_0\tilde{\sigma}\left(N, A_z + \frac{\partial\psi}{\partial z}\right)_\Omega = 0 \tag{17}$$

$$i\omega\mu_0(\tilde{\sigma}\nabla N, A)_\Omega + i\omega\mu_0(\tilde{\sigma}\nabla N, \nabla\psi)_\Omega = 0 \tag{18}$$

where $(u,\upsilon)_\Omega = \int_\Omega u\upsilon d\Omega$, $(\nabla u, \nabla\upsilon)_\Omega = \int_\Omega \nabla u\cdot\nabla\upsilon d\Omega$ and Ω is the whole space, and N is the linear nodal basis function (Jin 2002):

$$A_x^e = \sum_{i=1}^{8} A_{xi}^e N_i, A_y^e = \sum_{i=1}^{8} A_{yi}^e N_i, A_z^e = \sum_{i=1}^{8} A_{zi}^e N_i \tag{19}$$

$$\psi^e = \sum_{j=1}^{8} \psi_j^e N_j \tag{20}$$

After added the boundary conditions, the system equations can be obtained by the discretization of the differential equations:

$$\mathbf{Ku} = \mathbf{b} \tag{21}$$

The matrix for a given element can be expressed as:

$$\mathbf{K}_e = \begin{bmatrix} K_{11} & K_{12} \\ K_{21} & K_{22} \end{bmatrix}$$

$$= \sum_{i=1}^{8}\sum_{j=1}^{8} \begin{bmatrix} (-(\nabla N_i, \nabla N_j)_e & \\ +i\omega\mu_0(\tilde{\sigma}N_i, N_j)_e)I_{33} & i\omega\mu_0(\tilde{\sigma}N_i, \nabla N_j)_e \\ i\omega\mu_0(\tilde{\sigma}N_i, \nabla N_j)_e^T & i\omega\mu_0(\tilde{\sigma}\nabla N_i, \nabla N_j)_e \end{bmatrix} \tag{22}$$

where I_{33} is the 3×3 identity matrix. The values of $\mathbf{K}_e$ are given in Appendix A.

Boundary conditions

To obtain a unique solution for Equation (21), proper conditions must be imposed on the outer boundaries, including the top surface, the bottom surface and the four side surfaces of the study space utilised in this work; Dirichlet boundaries are adopted here. Assuming the outer boundaries are far enough from the anomalies,

$$\psi|_\Gamma = 0 \tag{23}$$

and

$$\mathbf{A}|_\Gamma = \frac{\mathbf{E}|_\Gamma}{i\omega} \tag{24}$$

Where $\mathbf{E}|_\Gamma$ is the solution corresponding to an earth model without any 2D or 3D conductivity anomalies. Two orthogonal sources are located on the top surface (ABCD).

Apparent resistivity and phase

According to Equations (4) and (5), the electric fields and magnetic fields can be obtained after solving Equation (21),

$$H_x = \frac{1}{\mu_0}\left(\frac{\partial A_z}{\partial y} - \frac{\partial A_y}{\partial z}\right), H_y = \frac{1}{\mu_0}\left(\frac{\partial A_x}{\partial z} - \frac{\partial A_z}{\partial x}\right),$$
$$H_z = \frac{1}{\mu_0}\left(\frac{\partial A_y}{\partial x} - \frac{\partial A_x}{\partial y}\right) \tag{25}$$

$$E_x = i\omega(A_x + \frac{\partial\psi}{\partial x}), E_y = i\omega(A_y + \frac{\partial\psi}{\partial y}),$$
$$E_z = i\omega(A_z + \frac{\partial\psi}{\partial z}) \tag{26}$$

Then, the apparent resistivities and phases can be obtained (Li 2002).

Numerical experiments

Validating the accuracy

To validate the correctness and accuracy of the algorithm presented in this paper, comparisons were made with results of the FD method (Pek and Verner 1997) for a 2D anisotropic model, and with solutions of the edge-based FE method (Xiao et al. 2018) for a 3D arbitrary anisotropic model, respectively.

2D test model

As shown in Figure 3, there is a 2D anisotropic anomaly in an anisotropic half-space. For the half-space, the principal conductivities are 0.005, 0.01 and 1/300 S/m, and its three Euler's angles are 30°, 0° and 0°, respectively. For the 2D anomaly, its principal conductivities are 1/60, 1/30 and 1/80 S/m, and its three Euler's angles are 10°, 60° and 20°, respectively; it has dimensions of 3600 m × 4400 m and its top depth is 410 m. Although the $\mathbf{A}-\psi$ method presented here is not suitable for 2D models because Dirichlet boundaries are adopted ($\psi|_\Gamma = 0$ should be satisfied at the outer boundaries), we used a 3D anomaly as an approximation of the 2D anomaly. Based on the 2D test model, what is different is that the 3D anomaly has a length of 40 000 m in the *x*-direction.

At a frequency of 50 Hz, we compared our results ($x = 0$ m) with the solutions of FD code (Pek and Verner 1997). As shown in Figure 3, the comparison reveals that the results of the two methods show very close levels of agreement.

3D test model

The 3D test anisotropic model is shown in Figure 5. In an isotropic half-space whose conductivity is 0.01 S/m, there is a 3D generally anisotropic anomaly whose dimensions are 600 m × 600 m × 600 m and top depth is 220 m. Its three Euler's angles ($\alpha_S, \alpha_D, \alpha_L$) are 10°, 30°

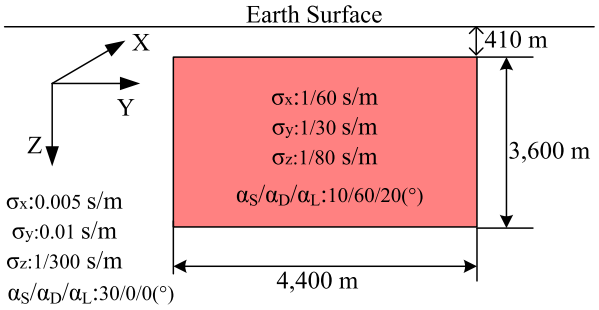

Figure 3. The 2D test model.

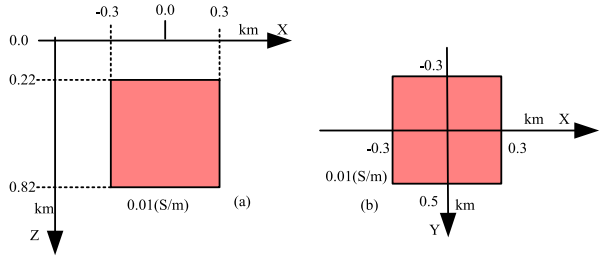

Figure 5. The 3D test model: (a) the left diagram is the section view; (b) the right diagram is the plan view.

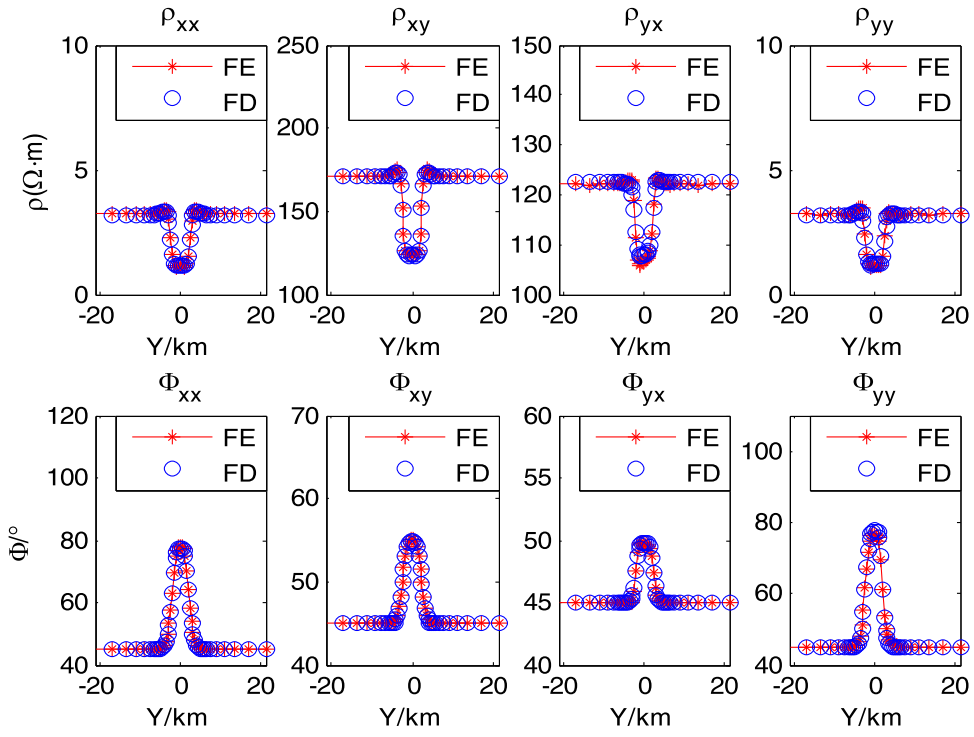

Figure 4. The comparison of A $-\psi$ method and the FD method (Pek and Verner 1997).

and 20°, respectively. Its three principal conductivities (σ_x, σ_y and σ_z) are 0.01, 0.02 and 0.005 S/m, respectively. The apparent resistivities of the two methods are shown in Figure 5. The compute frequency is 10 Hz.

In Figure 6, the first and second columns correspond to the apparent resistivities of the $\mathbf{A}-\psi$ method and edge-based FE method (Xiao et al. 2018), respectively; the third column corresponds to the relative errors (%); the first and second rows correspond to ρ_{xy} and ρ_{yx}, respectively. As shown in Figure 6, the results of the two methods reveal very close levels of agreement as the relative errors are $< 3\%$.

Sparsity patterns

Although the scale of the 3D test model is not large, it is suitable to analyse sparsity patterns and solvers. The sparsity patterns in different conditions are shown

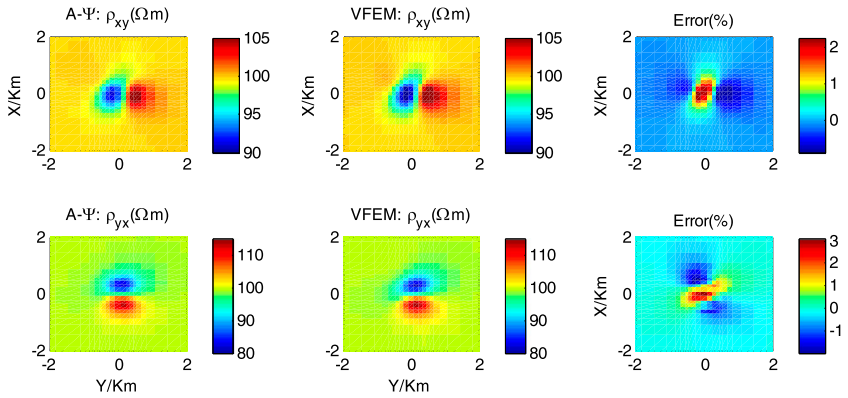

Figure 6. The comparison of the results of A $-\psi$ method and edge-based FE method (Xiao et al. 2018).

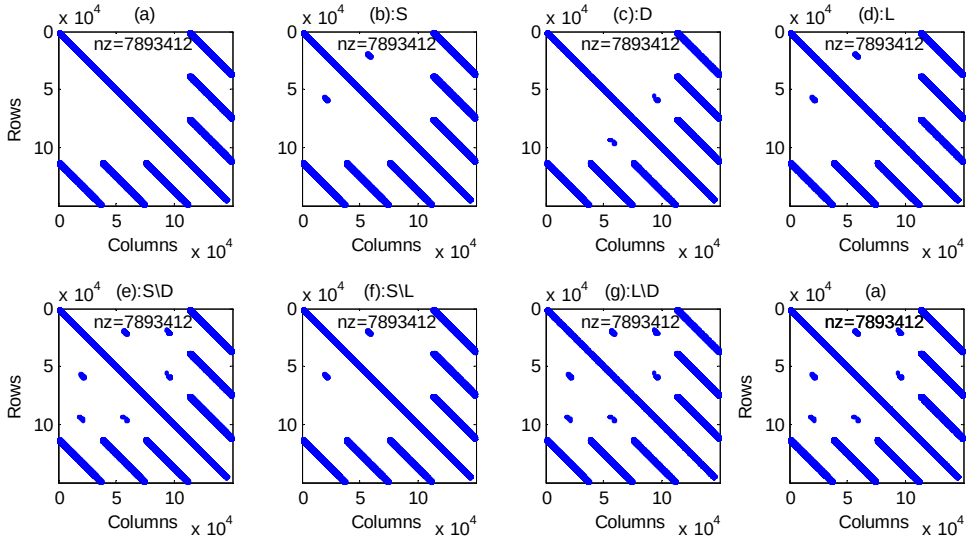

Figure 7. Sparsity patterns: (a) axial anisotropy; (b) $\alpha_S \neq 0$; (c) $\alpha_D \neq 0$; (d) $\alpha_L \neq 0$; (e) $\alpha_S \neq 0$ and $\alpha_D \neq 0$; (f) $\alpha_S \neq 0$ and $\alpha_L \neq 0$; (g) $\alpha_D \neq 0$ and $\alpha_L \neq 0$; (h) $\alpha_S \neq 0$, $\alpha_D \neq 0$ and $\alpha_L \neq 0$.

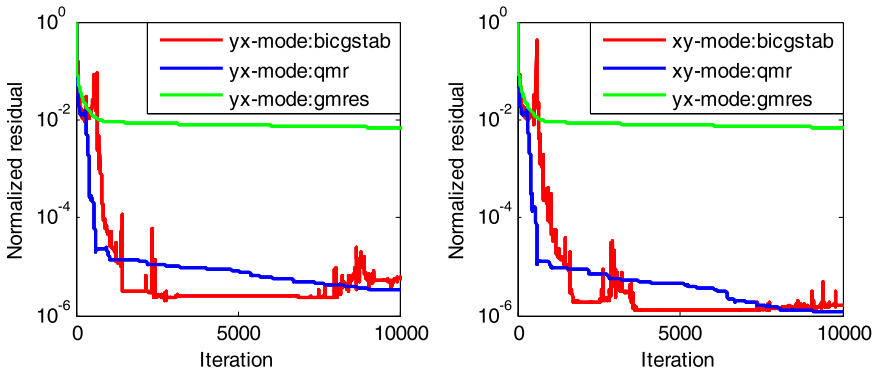

Figure 8. Convergences plot of QMR, BiCGSTAB and GMRES solvers without pre-conditioners for the data of the test model.

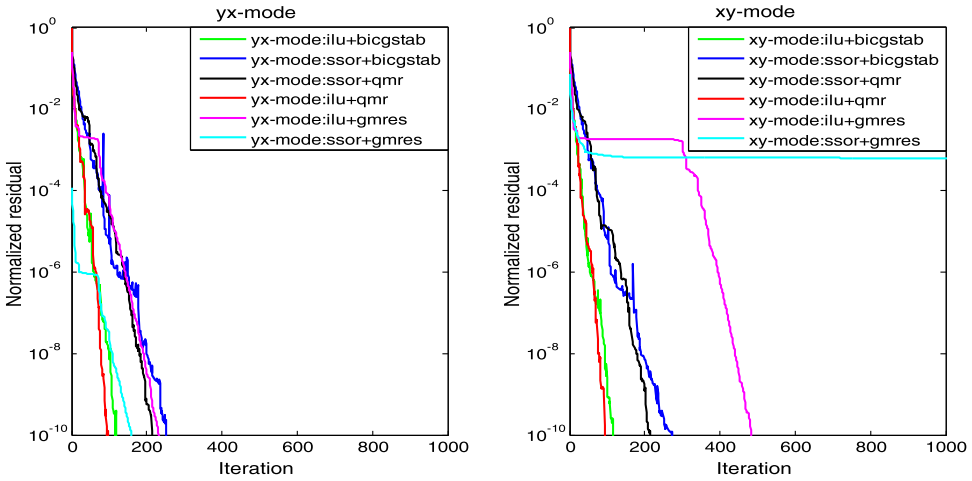

Figure 9. Convergences plot of QMR, BiCGSTAB and GMRES solvers with pre-conditioners for the data of the test model.

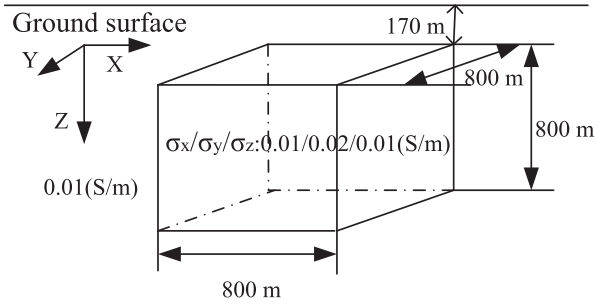

Figure 10. A 3D anisotropic body embedded in a half-space.

in Figure 7. The mesh contains 34 200 elements and 37 479 nodes. The resulting size of the sparse stiffness matrix is 149 916 × 149 916. The nonzero number is 7 893 412. As shown in Figure 7, the patterns change as the angles change. There are eight cases: (a) α_S, α_D and α_L all equal 0°; (b) α_S is nonzero but the other two Euler's angles both equal 0°; (c) α_D is nonzero but the other two Euler's angles both equal 0°; (d) α_L is nonzero but the other two Euler's angles both equal 0°; (e) α_S and α_D both are nonzero but α_L is 0°; (f) α_S and α_L both are nonzero but α_D equals 0°; (g) α_L and α_D both are nonzero but α_S is 0°; and (h) none of three Euler's angles

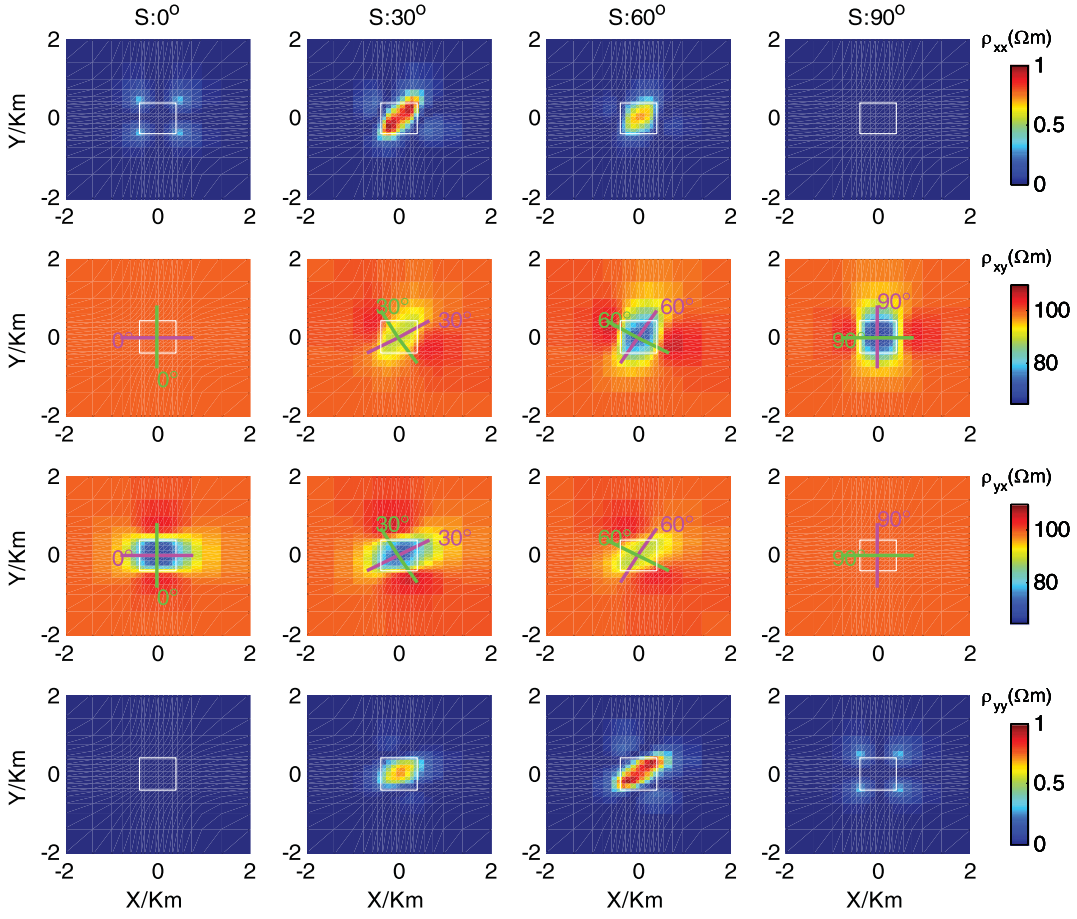

Figure 11. The apparent resistivities with a different angle α_S for the 3D model in Figure 10 at the frequency of 20 Hz.

is 0°. As shown in Figure 7, (b), (d) and (f) are similar to each other, and (e), (g) and (h) are similar to each other, which is in agreement with the theory shown in Figure 1.

Solvers and preconditioners

Figure 8 shows the convergences plot of quasi-mini mum residual (QMR), bi-conjugate gradient stabilised (BiCGSTAB) and generalised minimal residual (GMRES) solvers without preconditioners for the data of the 3D test model at the frequency of 10 Hz. For both the xy-mode and yx-mode, it shows clearly that QMR and BiCGSTAB solvers are more stable compared with the GMRES solver, and the convergence of GMRES is slower than that for the QMR solver and BiCGSTAB solver. However, up to 10 000 iterations, the convergences of the three solvers are $> 10^{-6}$.

Figure 9 shows the convergences plot of QMR, BiCGSTAB and GMRES solvers with symmetric successive over-relaxation (SSOR) or incomplete LU (ILU, where "LU" stands for lower upper) preconditioner. For both the xy-mode and yx-mode, it shows clearly that a QMR solver with ILU preconditioner and a BiCGSTAB solver with ILU preconditioner are more stable and faster compared with the other schemes. Because the results of the other models in this paper are similar, we show only the results of this 3D test model. Comparing Figure 8 with Figure 9, we find that it is very important to choose a proper preconditioner.

3D anisotropic model

To study the responses of MT in anisotropic media, based on previous work (Xiao et al. 2018), a special 3D anisotropic model is studied. As shown in Figure 10, a 3D anisotropic anomaly is embedded in an isotropic half-space of 0.01 S/m. The anomaly has a dimension of $800 \times 800 \times 800$ m, and a top depth of 170 m. For the three principal conductivities, σ_x and σ_z are both equal to 0.01 S/m, which is the same as the conductivity of the half-space, and σ_y is 0.02 S/m. Three cases with different Euler's angles are studied.

For the case of $\alpha_S = 0°/30°/60°/90°, \alpha_D = 0°, \alpha_L = 0°$, the apparent resistivities are shown in Figure 11. The angles α_D and α_L are both equal to 0°, and the angle α_S is

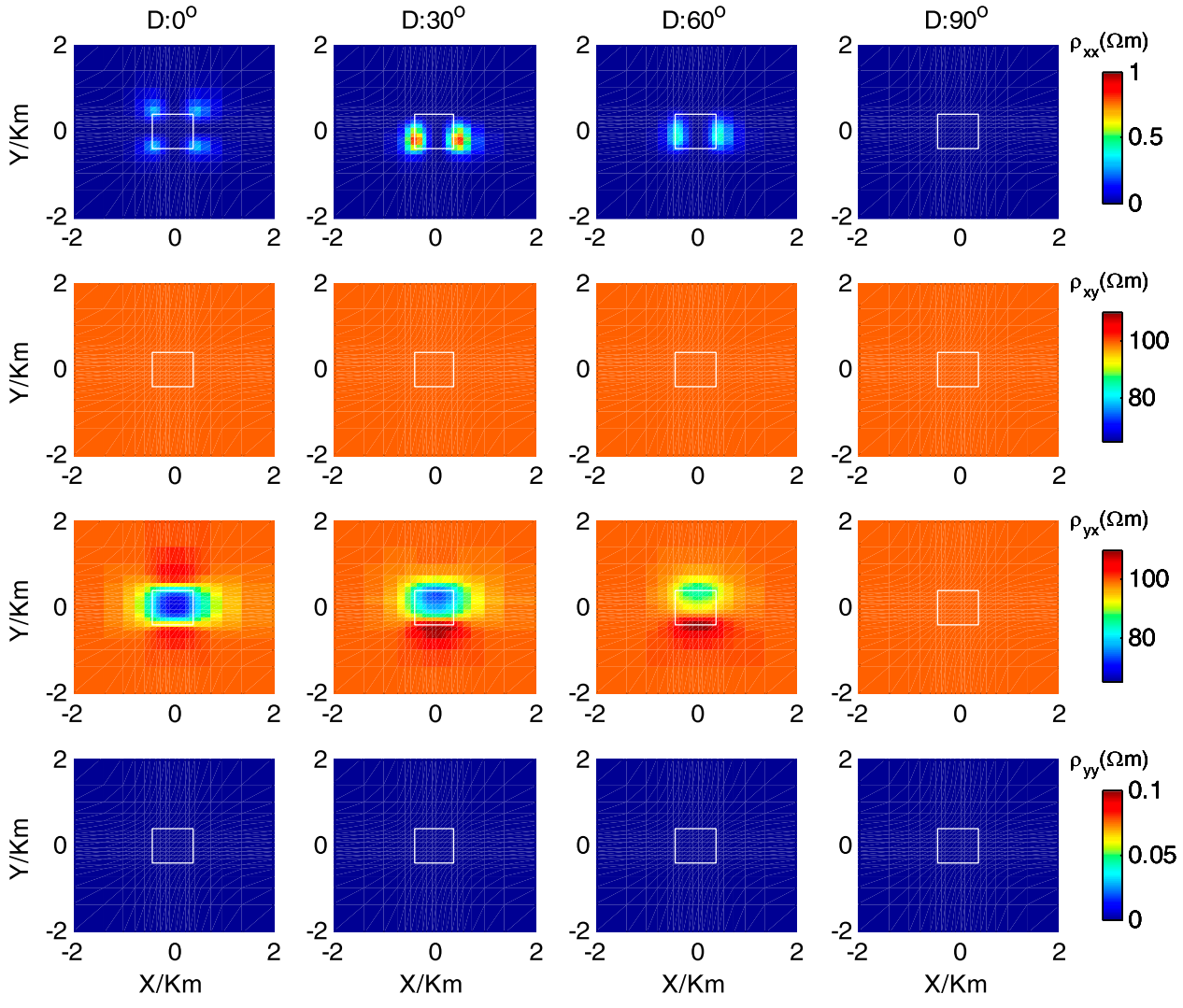

Figure 12. The apparent resistivities with a different angle α_D for 3D model in Figure 9 at the frequency of 20 Hz.

0°, 30°, 60° and 90° from left to right, respectively. There are three symbols used in Figure 11: the white square represents the shape and size of the anomalous body in the horizontal plane; the angles between the purple solid line and the x direction are 0°, 30°, 60° and 90° from left to right, respectively; and the angles between the green solid line and the y direction are 0°, 30°, 60° and 90° from left to right, respectively. The meanings of these three symbols remain unchanged in this paper. As shown in Figure 11, (1) when $\alpha_S = 0°$, $\rho_{xy} = 100\ \Omega \cdot m$ and $\rho_{yy} = 0\ \Omega \cdot m$, this is because the conductivity in the x-direction is 0.01 S/m and remains unchanged when $\alpha_S = 0°$; (2) because the conductivity in the y-direction remains unchanged with a value of 0.01 S/m when $\alpha_S = 90°$, $\rho_{yx} = 100\ \Omega \cdot m$ and $\rho_{xx} = 0\ \Omega \cdot m$; (3) when α_S is 0° or 90°, ρ_{xx}, ρ_{xy}, ρ_{yx} and ρ_{yy} all are symmetric; (4) as α_S changes, ρ_{xx}, ρ_{xy}, ρ_{yx} and ρ_{yy} all can indicate the position and shape of the anomalous body; (5) as α_S changes, ρ_{xy}, ρ_{yx} are able to indicate the value of angle α_S.

For the case of $\alpha_S = 0°, \alpha_D = 0°/30°/60°/90°, \alpha_L = 0°$, the apparent resistivities are shown in Figure 12. The angles α_S and α_L are both equal to 0°, and angle α_D is 0°, 30°, 60° and 90° from left to right, respectively. As shown in Figure 12: (1) when α_D changes, $\rho_{xy} = 100\ \Omega \cdot m$ and $\rho_{yy} = 0\ \Omega \cdot m$, this is because the conductivity in the x-direction remains unchanged with a value of 0.01 S/m; (2) when α_D is 90°, $\rho_{yx} = 100\ \Omega \cdot m$ and $\rho_{xx} = 0\ \Omega \cdot m$, as the conductivity in the y-direction is 0.01 S/m; (3) in this case, ρ_{xx} and ρ_{yx} both can indicate the position of the anomalous body, however, ρ_{xy} and ρ_{yy} cannot.

For the case of $\alpha_S = 0°, \alpha_D = 0°/30°/60°/90°, \alpha_L = 0°$, the apparent resistivities (ρ_{xx}, ρ_{xy}, ρ_{yx} and ρ_{yy}) are the same as the apparent resistivities in Figure 11, this is because angle α_S and angle α_L work in the same way when $\alpha_D = 0°$, which agrees with the theory shown in Figure 1.

Conclusions

In terms of Coulomb-gauged EM potentials, we developed a node-based FE algorithm for the MT numerical modelling in 3D conductivity anisotropic media. The accuracy of this algorithm was validated by comparing its results with solutions of the FD method for a 2D anisotropy model, and with solutions of the edge-based FE method for a 3D generalised anisotropy model, respectively. We then studied different solvers with different preconditioners. A simple 3D anisotropic model in three different conditions was then studied. Considering the results and discussion above, we reached four main conclusions: (1) when α_D and α_L both equal 0°, and $\alpha_S$changes, the apparent resistivity is able to indicate the position and shape of the anomalous body, furthermore, ρ_{xy} and ρ_{yx} can both indicate the value of α_S; (2) when α_S and α_L both equal 0°, and α_D changes, the conductivity in the x-direction remains unchanged, and the apparent resistivity can still indicate the position and shape of the anomalous body; (3) if a principal conductivity is in the x direction, then ρ_{xy} and ρ_{yy} almost remain the same, namely the conductivity in the y-direction or z-direction has almost no influence; (4) if a principal conductivity is in the y-direction, then ρ_{yx} and ρ_{xx} remain almost unchanged; (5) if a principal conductivity is in the z-direction, then it has almost no influence on the apparent resistivities. In addition, (6) for the total stiffness equation in this paper, QMR solver with the ILU preconditioner is more stable and faster comparing with the other schemes.

Acknowledgements

The authors would like to express their thanks to Dr Li Yuguo for his PhD dissertation, to Dr Kong Wenxin for discussion about the modelling of MT in 3D anisotropic media, and to Dr Josef Pek for his 1D and 2D FD codes. The authors declare no conflicts of interest.

Funding

This study is co-funded by the National Key Research and Development Project of China (2016YFC0600301) and the National Natural Science Foundation of China (No. 41425017).

References

Badea, E.A., M.E. Everett, G.A. Newman, and O. Biro. 2001. Finite-element analysis of controlled-source electromagnetic induction using Coulomb-gauged potentials. *Geophysics* 66 no. 3: 786–799. doi:10.1190/1.1444968.

Bai, D., M.J. Unsworth, M.A. Meju, X. Ma, J. Teng, X. Kong, and C. Zhao. 2010. Crustal deformation of the eastern Tibetan plateau revealed by magnetotelluric imaging. *Nature Geoscience* 3 no. 5: 358–362. doi.org/10.1038/ngeo830.

Biro, O., and K. Preis. 1989. On the use of the magnetic vector potential in the finite-element analysis of three-dimensional eddy currents. *IEEE Transactions on Magnetics* 25 no. 4: 3145–3159. doi:10.1109/20.34388.

Cai, H., B. Xiong, M. Han, and M. Zhdanov. 2014. 3D controlled-source electromagnetic modeling in anisotropic medium using edge-based finite element method. *Computers and Geosciences* 73: 164–176. doi:10.1016/j.cageo.2014.09.008.

Cai, H.Z., B. Xiong, and M. Zhdanov. 2015. Three-dimensional marine controlled-source electromagnetic modeling in anisotropic medium using finite element method. *Chinese Journal of Geophysics* 58 no. 8: 2839–2850. doi:10.6038/cjg20150818.

Cao, H., K. Wang, T. Wang, and B. Hua. 2018. Three-dimensional magnetotelluri axial anisotropic forward modeling and inversion. *Journal of Applied Geophysics*. doi:10.1016/j.jappgeo.2018.04.015.

Christensen, N.I. 1984. The magnitude, symmetry and origin of upper mantle anisotropy based on fabric analyses of ultramafic tectonites. *Geophysical Journal International* 76 no. 1: 89–111. doi:10.1111/j.1365-246X.1984.tb05025.x.

Dekker, D.L., and L.M. Hastie. 1980. Magneto-telluric impe dances of an anisotropic layered Earth model. *Geophysical Journal International* 61 no. 1: 11–20. doi:.

Evans, R.L., G. Hirth, K. Baba, D. Forsyth, A. Chave, and R. Mackie. 2005. Geophysical evidence from the MELT area for compositional controls on oceanic plates. *Nature* 437 no. 7056: 249. doi:10.1111/j.1365-246X.1980.tb04300.x.

Everett, M.E. 2012. Theoretical developments in electromagnetic induction geophysics with selected applications in the near surface. *Surveys in Geophysics* 33 no. 1: 29–63. doi:10.1007/s10712-011-9138-y.

Farquharson, C.G., and J.A. Craven. 2009. Three-dimensional inversion of magnetotelluric data for mineral exploration: An example from the McArthur River uranium deposit, Saskatchewan, Canada. *Journal of Applied Geophysics* 68 no. 4: 450–458. doi.org/10.1016/j.jappgeo.2008.02.002.

Haber, E., U.M. Ascher, D.A. Aruliah, and D.W. Oldenburg. 2000. Fast simulation of 3D electromagnetic problems using potentials. *Journal of Computational Physics* 163 no. 1: 150–171. doi:10.1006/jcph.2000.6545.

Häuserer, M., and A. Junge. 2011. Electrical mantle anisotropy and crustal conductor: a 3-D conductivity model of the Rwenzori Region in western Uganda. *Geophysical Journal International* 185 no. 3: 1235–1242. 10.1111/j.1365-246X.2011.05006.x.

Heise, W., and J. Pous. 2001. Effects of anisotropy on the two-dimensional inversion procedure. *Geophysical Journal International* 147 no. 3: 610–621. doi:10.1046/j.0956-540x.2001.01560.x.

Heise, W., and J. Pous. 2003. Anomalous phases exceeding 90° in magnetotellurics: anisotropic model studies and a field example. *Geophysical Journal International* 155 no. 1: 308–318. doi:10.1046/j.1365-246X.2003.02050.x.

Hu, X.Y., G.P. Huo, R. Gao, H.Y. Wang, Y.F. Huang, Y.X. Zhang, B.X. Zuo, and J.C. Cai. 2013. The magnetotelluric anisotropic two-dimensional simulation and case analysis. *Chinese Journal of Geophysics* 56 no. 12: 4268–4277. doi:10.6038/cjg20131229.

Huo, G.P., X.Y. Hu, Y.F. Huang, and B. Han. 2015. MT modeling for two-dimensional anisotropic conductivity structure with topography and examples of comparative analyses. *Chinese Journal of Geophysics* 58 no. 12: 4696–4708. doi:10.6038/cjg20151230.

Jin, J.M. 2002. *The finite element method in electromagnetics*. 2nd ed. New York: John Wiley and Sons.

Kirkby, A., G. Heinson, S. Holford, and S. Thiel. 2015. Mapping fractures using 1D anisotropic modelling of magnetotelluric data: A case study from the Otway Basin, Victoria, Australia. *Geophysical Journal International* 201 no. 3: 1961–1976. doi:10.1093/gji/ggv116.

Klein, K.A., and J.C. Santamarina. 2003. Electrical conductivity in soils: Underlying phenomena. *Journal of Environmental and Engineering Geophysics* 8 no. 4: 263–273. doi:10.4133/JEEG8.4.263.

Kong, W., C. Lin, H. Tan, M. Peng, T. Tong, and M. Wang. 2018. The effects of 3D electrical anisotropy on magnetotelluric responses: synthetic case studies. *Journal of Environmental and Engineering Geophysics* 23 no. 1: 61–75. doi:10.2113/JEEG23.1.61.

Li, J., G. Farquharson, and X. Hu. 2016. 3D vector finite-element electromagnetic forward modeling for large loop sources using a total-field algorithm and unstructured tetrahedral grids. *Geophysics* 82: E1–E16. doi.org/10.1190/geo2016-0004.1.

Li, Y. 2000. *Finite element modeling of electromagnetic fields in two-and three-dimensional anisotropic conductivity structures*. Ph.D. Thesis, University of Gottingen.

Li, Y. 2002. A finite-element algorithm for electromagnetic induction in two-dimensional anisotropic conductivity structures. *Geophysical Journal International* 148 no. 3: 389–401. doi:10.1046/j.1365-246x.2002.01570.x.

Li, Y., and J. Pek. 2008. Adaptive finite element modelling of two-dimensional magnetotelluric fields in general anisotropic media. *Geophysical Journal International* 175 no. 3: 942–954. doi:10.1111/j.1365-246X.2008.03955.x.

Liu, Y., Z. Xu, and Y. Li. 2018. Adaptive finite element modelling of three-dimensional magnetotelluric fields in general anisotropic media. *Journal of Applied Geophysics* 151: 113–124. doi:10.1016/j.jappgeo.2018.01.012.

Löwer, A., and A. Junge. 2017. Magnetotelluric transfer functions: phase tensor and tipper vector above a simple anisotropic three-dimensional conductivity anomaly and implications for 3Disotropic inversion. *Pure and Applied Geophysics* 174 no. 5: 2089–2101. doi:10.1007/s0002.

Martinelli, P., and A. Osella. 1997. MT forward modeling of 3-D anisotropic electrical conductivity structures using the Rayleigh-Fourier method. *Journal of geomagnetism and geoelectricity* 49 no. 11-12: 1499–1518. doi:10.5636/jgg.49.1499.

Mitsuhata, Y., and T. Uchida. 2004. 3D magnetotelluric modeling using the T-Ω finite-element method. *Geophysics* 69 no. 1: 108–119. doi:10.1190/1.1649380.

O'Brien, D.P., and H.F. Morrison. 1967. Electromagnetic fields in an n-layer anisotropic half-space. *Geophysics* 32 no. 4: 668–677. doi:10.1190/1.1439882.

Pek, J., and F.A. Santos. 2002. Magnetotelluric impedances and parametric sensitivities for 1-D anisotropic layered media. *Computers and Geosciences* 28 no. 8: 939–950. doi:10.1016/S0098-3004(02)00014-6.

Pek, J., and T. Verner. 1997. Finite-difference modelling of magnetotelluric fields in two-dimensional anisotropic media. *Geophysical Journal International* 128 no. 3: 505–521. doi:10.1111/j.1365-246X.1997.tb05314.x.

Puzyrev, V., J. Koldan, J. de la Puente, G. Houzeaux, M. Vázquez, and J.M. Cela. 2013. A parallel finite-element method for three-dimensional controlled-source electromagnetic forward modelling. *Geophysical Journal International* 193 no. 2: 678–693. doi:10.1093/gji/ggt027.

Reddy, I.K., and D. Rankin. 1971. Magnetotelluric effect of dipping anisotropies. *Geophysical Prospecting* 19 no. 1: 84–97. doi:10.1111/j.1365-2478.1971.tb00586.x.

Ren, Z.Y., T. Kalscheuer, S. Greenhalgh, and H. Maurer. 2014. A finite-element-based domain-decomposition approach for plane wave 3D electromagnetic modeling. *Geophysics* 79 no. 6: E255–E268. doi:10.1190/geo2013-0376.1.

Sarvandani, M.M., A.N. Kalateh, M. Unsworth, and A. Majidi. 2017. Interpretation of magnetotelluric data from the Gachsaran oil field using sharp boundary inversion. *Journal of Petroleum Science and Engineering* 149: 25–39. doi.org/10.1016/j.petrol.2016.10.019.

Wang, T., and S. Fang. 2001. 3-D electromagnetic anisotropy modeling using finite differences. *Geophysics* 66 no. 5: 1386–1398. doi:10.1190/1.1486779.

Weidelt, P., M. Oristaglio, and B. Spies. 1999. 3-D conductivity models: Implications of electrical anisotropy. *Three-dimensional Electromagnetics* 7: 119–137. doi:10.1190/1.9781560802154.ch8.

Xiao, T., H. Xiangyu, and W. Yun. 2018a. 3D MT modeling using the T–Ω method in general anisotropic media. *Journal of Applied Geophysics*. doi:10.1016/j.jappgeo.2018.11.012.

Xiao, T., Y. Liu, Y. Wang, and L.Y. Fu. 2018b. Three-dimensional magnetotelluric modeling in anisotropic media using edge-based finite element method. *Journal of Applied Geophysics* 149: 1–9. doi:10.1016/j.jappgeo.2017.12.009.

Xu, S.Z. 1994. *The Finite Element Methods in Geophysics*. Beijing, China: Science Press.

Yin, C. 2000. Geoelectrical inversion for a one-dimensional anisotropic model and inherent non-uniqueness. *Geophysical Journal International* 140 no. 1: 11–23. doi:10.1046/j.1365-246x.2000.00974.x.

Yin, C. 2003. Inherent nonuniqueness in magnetotelluric inversion for 1D anisotropic models. *Geophysics* 68 no. 1: 138–146. doi:10.1190/1.1543201.

Appendix A: the values of K_e

$$\mathbf{K}_e = \begin{bmatrix} K_{11} & K_{12} \\ K_{21} & K_{22} \end{bmatrix} = \sum_{i=1}^{8}\sum_{j=1}^{8} \begin{bmatrix} (-(\nabla N_i, \nabla N_j)_e & i\omega\mu_0(\tilde{\sigma} N_i, \nabla N_j)_e \\ +i\omega\mu_0(\tilde{\sigma} N_i, N_j)_e)I_{33} & \\ i\omega\mu_0(\tilde{\sigma} N_i, \nabla N_j)_e^T & i\omega\mu_0(\tilde{\sigma}\nabla N_i, \nabla N_j)_e \end{bmatrix} \tag{A1}$$

(1) K_{11}^e

$$K_{11}^e = \int_v \sum_{i=1}^{8}\sum_{j=1}^{8} \{-[A] + i\omega\mu_0[B]\} \mathrm{d}v \tag{A2}$$

where

$$A = \begin{pmatrix} \left[\frac{\partial N_i}{\partial x}\frac{\partial N_j}{\partial x} + \frac{\partial N_i}{\partial y}\frac{\partial N_j}{\partial y} + \frac{\partial N_i}{\partial z}\frac{\partial N_j}{\partial z}\right] & \mathbf{0} \\ \mathbf{0} & \left[\frac{\partial N_i}{\partial x}\frac{\partial N_j}{\partial x} + \frac{\partial N_i}{\partial y}\frac{\partial N_j}{\partial y} + \frac{\partial N_i}{\partial z}\frac{\partial N_j}{\partial z}\right] \\ \mathbf{0} & \mathbf{0} \\ & 0 \end{pmatrix} \begin{matrix} \mathbf{0} \\ \mathbf{0} \\ \left[\frac{\partial N_i}{\partial x}\frac{\partial N_j}{\partial x} + \frac{\partial N_i}{\partial y}\frac{\partial N_j}{\partial y} + \frac{\partial N_i}{\partial z}\frac{\partial N_j}{\partial z}\right] \end{matrix} \tag{A3}$$

$$B = \begin{pmatrix} N_i & 0 & 0 \\ 0 & N_i & 0 \\ 0 & 0 & N_i \end{pmatrix} \begin{pmatrix} \sigma_{xx} & \sigma_{xy} & \sigma_{xz} \\ \sigma_{yx} & \sigma_{yy} & \sigma_{yz} \\ \sigma_{zx} & \sigma_{zy} & \sigma_{zz} \end{pmatrix} \begin{pmatrix} N_j & 0 & 0 \\ 0 & N_j & 0 \\ 0 & 0 & N_j \end{pmatrix} = \begin{pmatrix} \sigma_{xx}[N_iN_j] & \sigma_{xy}[N_iN_j] & \sigma_{xz}[N_iN_j] \\ \sigma_{yx}[N_iN_j] & \sigma_{yy}[N_iN_j] & \sigma_{yz}[N_iN_j] \\ \sigma_{zx}[N_iN_j] & \sigma_{zy}[N_iN_j] & \sigma_{zz}[N_iN_j] \end{pmatrix} \tag{A4}$$

Therefore

$$K_{11}^e = \begin{pmatrix} -\frac{bc}{36a}K_{11a}^e - \frac{ac}{36b}K_{11b}^e & i\omega\sigma_{xz}\frac{abc}{216}K_{11d}^e \\ -\frac{ab}{36c}K_{11c}^e + i\omega\sigma_{xx}\frac{abc}{216}K_{11d}^e & i\omega\sigma_{xy}\frac{abc}{216}K_{11d}^e \\ i\omega\sigma_{yx}\frac{abc}{216}K_{11d}^e & i\omega\sigma_{yz}\frac{abc}{216}K_{11d}^e \\ & -\frac{bc}{36a}K_{11a}^e - \frac{ac}{36b}K_{11b}^e \\ & -\frac{ab}{36c}K_{11c}^e + i\omega\sigma_{yy}\frac{abc}{216}K_{11d}^e \\ i\omega\sigma_{zx}\frac{abc}{216}K_{11d}^e & i\omega\sigma_{zy}\frac{abc}{216}K_{11d}^e \end{pmatrix} \begin{matrix} i\omega\sigma_{xz}\frac{abc}{216}K_{11d}^e \\ i\omega\sigma_{yz}\frac{abc}{216}K_{11d}^e \\ -\frac{bc}{36a}K_{11a}^e - \frac{ac}{36b}K_{11b}^e - \frac{ab}{36c}K_{11c}^e + i\omega\sigma_{zz}\frac{abc}{216}K_{11d}^e \end{matrix} \tag{A5}$$

where

$$K_{11a}{}^e = \begin{bmatrix} 4 & -4 & -2 & 2 & 2 & -2 & -1 & 1 \\ -4 & 4 & 2 & -2 & -2 & 2 & 1 & -1 \\ -2 & 2 & 4 & -4 & -1 & 1 & 2 & -2 \\ 2 & -2 & -4 & 4 & 1 & -1 & -2 & 2 \\ 2 & -2 & -1 & 1 & 4 & -4 & -2 & 2 \\ -2 & 2 & 1 & -1 & -4 & 4 & 2 & -2 \\ -1 & 1 & 2 & -2 & -2 & 2 & 4 & -4 \\ 1 & -1 & -2 & 2 & 2 & -2 & -4 & 4 \end{bmatrix} \tag{A6}$$

$$K_{11b}^e = \begin{bmatrix} 4 & 2 & -2 & -4 & 2 & 1 & -1 & -2 \\ 2 & 4 & -4 & -2 & 1 & 2 & -2 & -1 \\ -2 & -4 & 4 & 2 & -1 & -2 & 2 & 1 \\ -4 & -2 & 2 & 4 & -2 & -1 & 1 & 2 \\ 2 & 1 & -1 & -2 & 4 & 2 & -2 & -4 \\ 1 & 2 & -2 & -1 & 2 & 4 & -4 & -2 \\ -1 & -2 & 2 & 1 & -2 & -4 & 4 & 2 \\ -2 & -1 & 1 & 2 & -4 & -2 & 2 & 4 \end{bmatrix} \tag{A7}$$

$$K_{11c}^e = \begin{bmatrix} 4 & 2 & 1 & 2 & -4 & -2 & -1 & -2 \\ 2 & 4 & 2 & 1 & -2 & -4 & -2 & -1 \\ 1 & 2 & 4 & 2 & -1 & -2 & -4 & -2 \\ 2 & 1 & 2 & 4 & -2 & -1 & -2 & -4 \\ -4 & -2 & -1 & -2 & 4 & 2 & 1 & 2 \\ -2 & -4 & -2 & -1 & 2 & 4 & 2 & 1 \\ -1 & -2 & -4 & -2 & 1 & 2 & 4 & 2 \\ -2 & -1 & -2 & -4 & 2 & 1 & 2 & 4 \end{bmatrix} \tag{A8}$$

$$K_{11d}^e = \begin{bmatrix} 8 & 4 & 2 & 4 & 4 & 2 & 1 & 2 \\ 4 & 8 & 4 & 2 & 2 & 4 & 2 & 1 \\ 2 & 4 & 8 & 4 & 1 & 2 & 4 & 2 \\ 4 & 2 & 4 & 8 & 2 & 1 & 2 & 4 \\ 4 & 2 & 1 & 2 & 8 & 4 & 2 & 4 \\ 2 & 4 & 2 & 1 & 4 & 8 & 4 & 2 \\ 1 & 2 & 4 & 2 & 2 & 4 & 8 & 4 \\ 2 & 1 & 2 & 4 & 4 & 2 & 4 & 8 \end{bmatrix} \tag{A9}$$

(2) K_{12}^e

$$K_{12}^e = \int_v i\omega\mu_0 \sum_{i=1}^{8}\sum_{j=1}^{8} [C] dv \tag{A10}$$

where

$$C = N_i \begin{pmatrix} \sigma_{xx} & \sigma_{xy} & \sigma_{xz} \\ \sigma_{yx} & \sigma_{yy} & \sigma_{yz} \\ \sigma_{zx} & \sigma_{zy} & \sigma_{zz} \end{pmatrix} \begin{pmatrix} \frac{\partial N_j}{\partial x} \\ \frac{\partial N_j}{\partial y} \\ \frac{\partial N_j}{\partial z} \end{pmatrix} = \begin{pmatrix} \sigma_{xx}\left[N_i\frac{\partial N_j}{\partial x}\right] + \sigma_{xy}\left[N_i\frac{\partial N_j}{\partial y}\right] + \sigma_{xz}\left[N_i\frac{\partial N_j}{\partial z}\right] \\ \sigma_{yx}\left[N_i\frac{\partial N_j}{\partial x}\right] + \sigma_{yy}\left[N_i\frac{\partial N_j}{\partial y}\right] + \sigma_{yz}\left[N_i\frac{\partial N_j}{\partial z}\right] \\ \sigma_{zx}\left[N_i\frac{\partial N_j}{\partial x}\right] + \sigma_{zy}\left[N_i\frac{\partial N_j}{\partial y}\right] + \sigma_{zz}\left[N_i\frac{\partial N_j}{\partial z}\right] \end{pmatrix} \tag{A11}$$

therefore

$$K_{12}^e = i\omega\mu_0 \begin{pmatrix} \frac{bc}{72}\sigma_{xx}K_{12a}^e + \frac{ac}{72}\sigma_{xy}K_{12b}^e + \frac{ab}{72}\sigma_{xz}K_{12c}^e \\ \frac{bc}{72}\sigma_{yx}K_{12a}^e + \frac{ac}{72}\sigma_{yy}K_{12b}^e + \frac{ab}{72}\sigma_{yz}K_{12c}^e \\ \frac{bc}{72}\sigma_{zx}K_{12a}^e + \frac{ac}{72}\sigma_{zy}K_{12b}^e + \frac{ab}{72}\sigma_{zz}K_{12c}^e \end{pmatrix} \tag{A12}$$

where

$$K_{12a}^e = \begin{bmatrix} -4 & 4 & 2 & -2 & -2 & 2 & 1 & -1 \\ -4 & 4 & 2 & -2 & -2 & 2 & 1 & -1 \\ -2 & 2 & 4 & -4 & -1 & 1 & 2 & -2 \\ -2 & 2 & 4 & -4 & -1 & 1 & 2 & -2 \\ -2 & 2 & 1 & -1 & -4 & 4 & 2 & -2 \\ -2 & 2 & 1 & -1 & -4 & 4 & 2 & -2 \\ -1 & 1 & 2 & -2 & -2 & 2 & 4 & -4 \\ -1 & 1 & 2 & -2 & -2 & 2 & 4 & -4 \end{bmatrix} \tag{A13}$$

$$K_{12b}^{e}=\begin{bmatrix}-4&-2&2&4&-2&-1&1&2\\-2&-4&4&2&-1&-2&2&1\\-2&-4&4&2&-1&-2&2&1\\-4&-2&2&4&-2&-1&1&2\\-2&-1&1&2&-4&-2&2&4\\-1&-2&2&1&-2&-4&4&2\\-1&-2&2&1&-2&-4&4&2\\-2&-1&1&2&-4&-2&2&4\end{bmatrix} \tag{A14}$$

$$K_{12c}^{e}=\begin{bmatrix}-4&-2&-1&-2&4&2&1&2\\-2&-4&-2&-1&2&4&2&1\\-1&-2&-4&-2&1&2&4&2\\-2&-1&-2&-4&2&1&2&4\\-4&-2&-1&-2&4&2&1&2\\-2&-4&-2&-1&2&4&2&1\\-1&-2&-4&-2&1&2&4&2\\-2&-1&-2&-4&2&1&2&4\end{bmatrix} \tag{A15}$$

(3) K_{21}^{e}

$$K_{21}^{e}=K_{12}^{e\,T} \tag{A16}$$

(4) K_{22}^{e}

$$K_{22}^{e}=\int_{v} i\omega\mu_0\sum_{i=1}^{8}\sum_{j=1}^{8}[D]dv \tag{A17}$$

where

$$\begin{aligned}D&=\begin{pmatrix}\frac{\partial N_i}{\partial x}&\frac{\partial N_i}{\partial y}&\frac{\partial N_i}{\partial z}\end{pmatrix}\begin{pmatrix}\sigma_{xx}&\sigma_{xy}&\sigma_{xz}\\\sigma_{yx}&\sigma_{yy}&\sigma_{yz}\\\sigma_{zx}&\sigma_{zy}&\sigma_{zz}\end{pmatrix}\begin{pmatrix}\frac{\partial N_j}{\partial x}\\\frac{\partial N_j}{\partial y}\\\frac{\partial N_j}{\partial z}\end{pmatrix}\\&=(\sigma_{xx}+\sigma_{yx}+\sigma_{zx})\left[\frac{\partial N_i}{\partial x}\frac{\partial N_j}{\partial x}\right]+(\sigma_{xy}+\sigma_{yy}+\sigma_{zy})\\&\left[\frac{\partial N_i}{\partial y}\frac{\partial N_j}{\partial y}\right]+(\sigma_{xz}+\sigma_{yz}+\sigma_{zz})\left[\frac{\partial N_i}{\partial z}\frac{\partial N_j}{\partial z}\right]\end{aligned} \tag{A18}$$

therefore

$$\begin{aligned}K_{22}^{e}=i\omega\mu_0\Bigg(&\sigma_{xx}\left[\frac{\partial N_i}{\partial x}\frac{\partial N_j}{\partial x}\right]+\sigma_{yx}\left[\frac{\partial N_i}{\partial y}\frac{\partial N_j}{\partial x}\right]+\\&\sigma_{zx}\left[\frac{\partial N_i}{\partial z}\frac{\partial N_j}{\partial x}\right]+\sigma_{xy}\left[\frac{\partial N_i}{\partial x}\frac{\partial N_j}{\partial y}\right]+\sigma_{yy}\left[\frac{\partial N_i}{\partial y}\frac{\partial N_j}{\partial y}\right]\\&+\sigma_{zy}\left[\frac{\partial N_i}{\partial z}\frac{\partial N_j}{\partial y}\right]+\sigma_{xz}\left[\frac{\partial N_i}{\partial x}\frac{\partial N_j}{\partial z}\right]\\&+\sigma_{yz}\left[\frac{\partial N_i}{\partial y}\frac{\partial N_j}{\partial x}\right]+\sigma_{zz}\left[\frac{\partial N_i}{\partial z}\frac{\partial N_j}{\partial z}\right]\Bigg)\end{aligned} \tag{A19}$$

where

$$K_{22a}^{e}=\begin{bmatrix}4&-4&-2&2&2&-2&-1&1\\-4&4&2&-2&-2&2&1&-1\\-2&2&4&-4&-1&1&2&-2\\2&-2&-4&4&1&-1&-2&2\\2&-2&-1&1&4&-4&-2&2\\-2&2&1&-1&-4&4&2&-2\\-1&1&2&-2&-2&2&4&-4\\1&-1&-2&2&2&-2&-4&4\end{bmatrix} \tag{A20}$$

$$K_{22b}^{e}=\begin{bmatrix}6&-6&-6&6&3&-3&-3&3\\6&-6&-6&6&3&-3&-3&3\\-6&6&6&-6&-3&3&3&-3\\-6&6&6&-6&-3&3&3&-3\\3&-3&-3&3&6&-6&-6&6\\3&-3&-3&3&6&-6&-6&6\\-3&3&3&-3&-6&6&6&-6\\-3&3&3&-3&-6&6&6&-6\end{bmatrix} \tag{A21}$$

$$K_{22c}^{e}=\begin{bmatrix}6&-6&-3&3&6&-6&-3&3\\6&-6&-3&3&6&-6&-3&3\\3&-3&-6&6&3&-3&-6&6\\3&-3&-6&6&3&-3&-6&6\\-6&6&3&-3&-6&6&3&-3\\-6&6&3&-3&-6&6&3&-3\\-3&3&6&-6&-3&3&6&-6\\-3&3&6&-6&-3&3&6&-6\end{bmatrix} \tag{A22}$$

$$K_{22d}^{e}=\begin{bmatrix}6&6&-6&-6&3&3&-3&-3\\-6&-6&6&6&-3&-3&3&3\\-6&-6&6&6&-3&-3&3&3\\6&6&-6&-6&3&3&-3&-3\\3&3&-3&-3&6&6&-6&-6\\-3&-3&3&3&-6&-6&6&6\\-3&-3&3&3&-6&-6&6&6\\3&3&-3&-3&6&6&-6&-6\end{bmatrix} \tag{A23}$$

$$K_{22e}^{e}=\begin{bmatrix}4&2&-2&-4&2&1&-1&-2\\2&4&-4&-2&1&2&-2&-1\\-2&-4&4&2&-1&-2&2&1\\-4&-2&2&4&-2&-1&1&2\\2&1&-1&-2&4&2&-2&-4\\1&2&-2&-1&2&4&-4&-2\\-1&-2&2&1&-2&-4&4&2\\-2&-1&1&2&-4&-2&2&4\end{bmatrix} \tag{A24}$$

$$K_{22f}^{e}=\begin{bmatrix}6&3&-3&-6&6&3&-3&-6\\3&6&-6&-3&3&6&-6&-3\\3&6&-6&-3&3&6&-6&-3\\6&3&-3&-6&6&3&-3&-6\\-6&-3&3&6&-6&-3&3&6\\-3&-6&6&3&-3&-6&6&3\\-3&-6&6&3&-3&-6&6&3\\-6&-3&3&6&-6&-3&3&3\end{bmatrix} \tag{A25}$$

$$K_{22g}^{e}=\begin{bmatrix}6&6&3&3&-6&-6&-3&-3\\-6&-6&-3&-3&6&6&3&3\\-3&-3&-6&-6&3&3&6&6\\3&3&6&6&-3&-3&-6&-6\\6&6&3&3&-6&-6&-3&-3\\-6&-6&-3&-3&6&6&3&3\\-3&-3&-6&-6&3&3&6&6\\3&3&6&6&-3&-3&-6&-6\end{bmatrix} \tag{A26}$$

$$K_{22h}^{e}=\begin{bmatrix}6&3&3&6&-6&-3&-3&-6\\3&6&6&3&-3&-6&-6&-3\\-3&-6&-6&-3&3&6&6&3\\-6&-3&-3&-6&6&3&3&6\\6&3&3&6&-6&-3&-3&-6\\3&6&6&3&-3&-6&-6&-3\\-3&-6&-6&-3&3&6&6&3\\-6&-3&-3&-6&6&3&3&6\end{bmatrix} \tag{A27}$$

$$K_{22i}^{e}=\begin{bmatrix}4&2&1&2&-4&-2&-1&-2\\2&4&2&1&-2&-4&-2&-1\\1&2&4&2&-1&-2&-4&-2\\2&1&2&4&-2&-1&-2&-4\\-4&-2&-1&-2&4&2&1&2\\-2&-4&-2&-1&2&4&2&1\\-1&-2&-4&-2&1&2&4&2\\-2&-1&-2&-4&2&1&2&4\end{bmatrix} \tag{A28}$$